HHS Public Access

Author manuscript

Anal Chem. Author manuscript; available in PMC 2024 August 01.

Published in final edited form as:

Anal Chem. 2023 August 01; 95(30): 11365–11374. doi:10.1021/acs.analchem.3c01539.

Phasor Representation Approach for Rapid Exploratory Analysis of Large Infrared Spectroscopic Imaging Data Sets

Sudipta S. Mukherjee,

Beckman Institute for Advanced Science and Technology, University of Illinois Urbana-Champaign, Urbana, Illinois 61801, United States

Rohit Bhargava

Beckman Institute for Advanced Science and Technology, Department of Bioengineering, Department of Chemical and Biomolecular Engineering, Department of Electrical and Computer Engineering, Mechanical Science and Engineering, and Cancer Center at Illinois, University of Illinois Urbana-Champaign, Urbana, Illinois 61801, United States

Abstract

Infrared (IR) spectroscopic imaging is potentially useful for digital histopathology as it provides spatially resolved molecular absorption spectra, which can subsequently yield useful information by powerful artificial intelligence methods. A typical analysis pipeline in using IR imaging data for chemical pathology often involves iterative processes of segmentation, evaluation, and analysis that necessitate rapid data exploration. Here, we present a fast, reliable, and intuitive method based on a phasor representation of spectra and discuss its unique applicability for IR imaging data. We simulate different features extant in IR spectra and discuss their influence on the phasor waveforms; similarly, we undertake IR image analysis in the transform space to understand spectral similarity and variance. We demonstrate the potential of phasor analysis for biomedical tissue imaging using a variety of samples, using fresh frozen surgical prostate resections and formalin-fixed paraffin-embedded breast cancer tissue microarray samples as model systems that span common histopathology practice. To demonstrate further generalizability of this approach, we apply the method to data from different experimental conditions—including standard (5.5 μm × 5.5 μm pixel size) and high-definition (1.1 μm × 1.1 μm pixel size) Fourier transform IR (FTIR) spectroscopic imaging using transmission and transflection modes. Quantitative segmentation results from our approach are compared to previous studies, showing good agreement and quick visualization. The presented method is rapid, easy to use, and highly capable of deciphering compositional differences, presenting a convenient tool for exploratory analysis of IR imaging data.

Corresponding Author Rohit Bhargava – Beckman Institute for Advanced Science and Technology, Department of Bioengineering, Department of Chemical and Biomolecular Engineering, Department of Electrical and Computer Engineering, Mechanical Science and Engineering, and Cancer Center at Illinois, University of Illinois Urbana-Champaign, Urbana, Illinois 61801, United States; rxb@illinois.edu.

The authors declare no competing financial interest.

ASSOCIATED CONTENT

Supporting Information

The Supporting Information is available free of charge at https://pubs.acs.org/doi/10.1021/acs.analchem.3c01539.

Phasor histogram for a higher phasor frequency, effect of MNF de-noising on the phasor histogram and classified image, and description of the method for choosing phasor frequencies for breast tissue classification (PDF)

Graphical Abstract

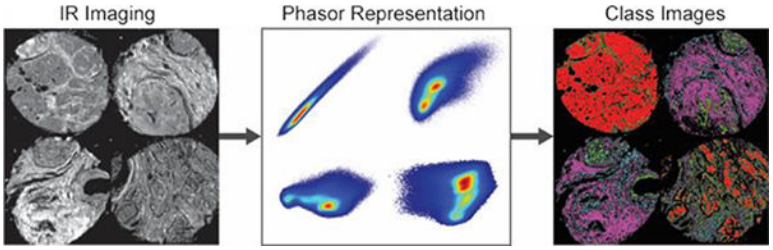

INTRODUCTION

Infrared (IR) spectroscopic imaging has greatly advanced as a tool for examining tissues with the development of fast acquisition approaches using array detectors, laser sources, custom-built optical assemblies, and the emergence of lower-cost analytic and storage capabilities to handle big data.[1–4] The differentiating feature of IR imaging from other tissue analysis techniques is that the imaging contrast arises from the relative proportions of different chemical species (proteins, lipids, DNA, etc.), which have rich and unique spectral signatures. Several studies have shown that different histologic classes in tissues (cell types, extracellular matrix, and deposits) are different in their IR spectral absorption patterns that arise from the inherent differences of chemical compositions. Hence, tissue organization and the presence of disease can potentially be detected without any extrinsic labeling. While the potential is exciting, one limitation to discovery and development of IR imaging for pathology arises from the size of IR imaging datasets. In order to meaningfully interpret IR images, analytical and machine learning (ML) methods have been developed, which have been reviewed elsewhere.[1] A common feature of all these methods is the need for dimensionality reduction of IR images. Briefly, the hyperdimensional IR imaging dataset is reduced to a smaller set before training ML models for ease of data handling, to manage the size and diversity of samples, and for speed in evaluation. Often, these approaches are limited in their potential for discovery. Carefully curated spectral metrics by experts may miss some key features of the data, especially finer and more subtle features, whereas variance focused methods like principal component analysis (PCA) can be influenced by large changes such as scattering-induced baseline variations, limited diversity of samples, sample morphology, or artifacts. In addition to reducing the computational time and storage requirements, dimensionality reduction is also necessary to prevent overfitting or influencing the data by chance and biases when it is impractical to acquire large datasets (preclinical studies and histopathology of rare diseases). Herein, we describe a visual phasor representation approach and its utility for rapidly examining high-dimensional data.

The phasor-based approach was used to analyze AC circuits,[5] adapted for fluorescence microscopy,[6] and has subsequently been utilized to study a wide range of imaging data, namely, time-resolved and spectrally resolved fluorescence,[7–9] stimulated Raman scattering microscopy,[10] ultrafast pump–probe[11] and MRI imaging.[12] At the heart of this approach is a Fourier series representation of a signal which enables simple visual representation, such as fluorescence lifetime, pump–probe, or T_1 (T_2) lifetimes in MRI. While originally related to explicit physical phenomena, namely, representing the magnitude and directional

relationship between two or more alternating quantities, the approach can be generalized to multiple species with individual characteristics. In particular, this approach is useful to rapidly identify clusters and locations of chemically similar regions in an image.[7] Herein, we seek a similar phasor representation of IR spectra with the aim of dimensionality reduction of large-bandwidth IR images. Fourier transforms have been applied to IR spectra for deconvolution (Fourier self-deconvolution),[13,14] calculating derivatives,[15] and for scattering correction;[16] however, they have not been reported for iterative exploratory analysis or image segmentation, which we seek to demonstrate in this study. Specifically, we seek to develop a pipeline for data visualization and assess whether the rapid insight afforded by this method can be useful for exploratory analyses in histopathology.

EXPERIMENTAL SECTION

The images used in this study are from fresh frozen (FF) prostate surgical resections (Mayo Clinic, Rochester, MN) and formalin-fixed paraffin-embedded (FFPE) breast cancer tissue microarray (TMA) sections obtained from US Biomax, Inc. (BR1003). The FF sections are from patients with various Gleason grades, typically 1.5 cm × 1.5 cm in size. The FFPE sample set consists of 101 cores of approximately 1 mm diameter each and sampled from 47 patients. All patient information was de-identified, and the study was approved by UIUC and Mayo Clinic institutional review boards. IR images were acquired either in transflection mode for prostate tissue thin sections deposited on low-e substrates[17] or in transmission mode for breast tissue thin sections deposited on the BaF_2 substrate. The imaging parameters for this dataset were either 5.5 or 1.1 μm pixel size and 4 cm^{-1} spectral resolution in the 0–3950 cm^{-1} (truncated to 900–3800 cm^{-1}) range, which are typical for an FTIR imaging spectrometer (Cary 600 Series, Agilent). Data were averaged for 4 co-adds for 5.5 μm, 16 co-adds for 1.1 μm, and 120 co-adds for background. Rubber-band baseline correction and minimum noise fraction (MNF) de-noising[18] were performed, and the effects of these will be discussed in detail under the Results and Discussion section and Supporting Information. For the methods described in this text, we used the inverse fast Fourier transform (IFFT) function in MATLAB (MathWorks) without any apodization function, and the spectral data were zero-padded by 4× (total points, $N = 4096$), as is routinely done in FT spectroscopy.[15] For evaluation of our approach, we compared our results with published results on the same sample (BR1003).[19] For the supervised classification results presented in this paper, the ground truth used in the original study for histologic classes (~70,000 pixels) annotated under the expert supervision of a pathologist was used.

RESULTS AND DISCUSSION

First, we provide the mathematical details and illustrate the salient aspects of our approach using synthetic IR spectra. The phasor transform involves calculating the real and imaginary parts of the inverse Fourier transform of the spectral data, which are defined in eqs 1 and 2, respectively:

$$u(k,x,y) = Re\left(\int_{-\infty}^{\infty} A(\tilde{v},x,y)e^{2\pi i k\tilde{v}}\,d\tilde{v}\right) \quad (1)$$

$$v\left(k,x,y\right)=\mathrm{Im}\left(\int_{-\infty}^{\infty}A\left(\tilde{v},x,y\right)\mathrm{e}^{2\pi ik\tilde{v}}\,\mathrm{d}\tilde{v}\right) \tag{2}$$

where x and y are the pixel indices, respectively, $\tilde{v}$ is the frequency in wavenumber (cm^{-1}), $A(\tilde{v},x,y)$ is the absorbance at each pixel, and k is the conjugate variable of wavenumber, often referred to as the spatial frequency. [14] However, since we are looking at images, to avoid any confusion with spatial features of the images, we call these the "phasor frequencies" in all subsequent discussions (and do not label the units in cm to avoid confusion with the spatial dimensions of images). From these transformations, the phasor can be defined as the vector

$$\overrightarrow{P}(k,x,y)=u(k,x,y)\hat{x}+v(k,x,y)\hat{y} \tag{3}$$

Although the phasor representation is a well-known concept, we present spectral components that can be considered building blocks for common biomedical IR spectra and whose inverse Fourier transform can be evaluated analytically (eqs 4–7) as these have direct implications for the development of our approach and spectral analyses. Underpinning our attempt to develop an understanding is that IR absorption is linear in the number of species, their interactions and environment; hence, complex spectral features can be understood as the linear combination of contributory IR absorption features of specific vibrational modes, and any spectrum can be expressed in terms of these elementary building blocks. Lorentzian and Gaussian band shapes[20] are the elementary curves that characterize absorption bands in IR spectroscopy. Their line shapes and analytical phasor representations, respectively, are given by the pairs of expressions

$$A(\tilde{v})=A\frac{\gamma^2}{\gamma^2+4(\tilde{v}-\tilde{v}_0)^2} \tag{4a}$$

$$\overrightarrow{P}(k)=\frac{\gamma A}{4}\cos(2\pi k\tilde{v}_0)\,\mathrm{e}^{-(\pi\gamma|k|)}\hat{x}+A\sin(2\pi k\tilde{v}_0)\,\mathrm{e}^{-(\pi\gamma|k|)}\hat{y} \tag{4b}$$

and

$$A(\tilde{v})=A\mathrm{e}^{-(\tilde{v}-\tilde{v}_0)^2/\sigma^2} \tag{5a}$$

$$\vec{P}(k) = A\sigma\sqrt{\pi}\cos(2\pi k\tilde{\nu}_0)\mathrm{e}^{-(\pi k\sigma)^2}\hat{x} + A\sigma\sqrt{\pi}\sin(2\pi k\tilde{\nu}_0)\mathrm{e}^{-(\pi k\sigma)^2}\hat{y} \quad (5b)$$

where $\tilde{\nu}_0$ is the central frequency of the band, A is the peak absorbance, 2γ is the full width at half-maximum (FWHM) of the Lorentzian, and σ is the width of the Gaussian distribution. While both of these are symmetric frequency distributions, it is well known that biological macromolecules, especially in media such as aqueous solutions, show a distribution of vibrational frequencies that is asymmetric. Fortunately, the asymmetry can also be included in simple modifications to the standard Lorentzian and Gaussian band shapes. [21] The impact of instrumental line shape on spectral data and that of optical effects on IR spectra of morphologically heterogeneous samples measured in a microscope are also known to influence the band shapes. [22,23] Without loss of generality, our approach can be extended to these special cases with the appropriate perturbation functions. Lorentzian and Gaussian band shapes are shown in Figure 1A,D, where the chosen peak position of the amide I vibrational mode (~1650 cm^{-1}) and an FWHM of 40 cm^{-1} are characteristic of protein absorption. As expected from the inverse Fourier transform formulae (eqs 4b and 5b), u (and v) are oscillatory functions with an exponential or Gaussian envelope (Figure 1B,E). Consequently, the trajectory of $\vec{P}(k)$ takes the form of a spiral decay, governed by the functional form of the band shape, its width, and central frequency (Figure 1C,F). Since the inverse Fourier transform of a real function has to be Hermitian, the negative k values carry no new information and are discarded without any loss of information content for all subsequent results presented in this paper.

A perturbation to the isolated band shape, for example, due to a subpopulation experiencing environmental interactions, can be represented by the Dirac delta function, and its phasor representation can be given as

$$A(\tilde{\nu}) = A\delta(\tilde{\nu} - \tilde{\nu}_0) \quad (6a)$$

and

$$\vec{P}(k) = A\cos(2\pi k\tilde{\nu}_0)\hat{x} + A\sin(2\pi k\tilde{\nu}_0)\hat{y} \quad (6b)$$

The phasor transformation extends the influence of this sharp, isolated feature throughout the phasor frequency domain, thus providing a means to visualize small but influential changes (Figure 1G–I). Since biomedical spectroscopy is composed of small changes between cells and disease states, an increased ability to observe the impacts of small changes may be beneficial. Two Dirac delta functions lead to the familiar beat pattern. For example, the sum of two Dirac delta functions of equal intensity

$$A(\tilde{\nu}) = A\delta(\tilde{\nu} - \tilde{\nu}_1) + A\delta(\tilde{\nu} - \tilde{\nu}_2) \tag{7a}$$

results in a waveform after the phasor transformation (shown in Figure 1J–L) as

$$\overrightarrow{P}(k) = 2A\cos(2\pi k\langle\tilde{\nu}\rangle)\cos(2\pi k\delta\tilde{\nu})\hat{x} + 2A\sin(2\pi k\langle\tilde{\nu}\rangle)\cos(2\pi k\delta\tilde{\nu})\hat{y} \tag{7b}$$

where $\langle\tilde{\nu}\rangle = \frac{(\tilde{\nu}_1 + \tilde{\nu}_2)}{2}$ and $\delta\tilde{\nu} = (\tilde{\nu}_1 - \tilde{\nu}_2)$.

A model for the absorbance, $A(\tilde{\nu})$, observed for biomedical spectra can be understood by ignoring scattering and assuming Lambert-Beer's law for weak absorption as $A(\tilde{\nu}) = \sum_l c_l\varepsilon_1(\tilde{\nu})L$, where c_l is the concentration of the lth chemical species (proteins, lipids, nucleic acids, carbohydrates, etc.) in that pixel, $\varepsilon_l(\tilde{\nu})$ is the molar extinction coefficient of the lth species, and L is the path length. For IR spectroscopy, we can write the following general expression for $\varepsilon_l(\tilde{\nu}) = \sum_{m(l)}^{M(l)} A_{m(l)}g(\tilde{\nu} - \tilde{\upsilon}_{m(l)})$, where $A_{m(l)}$ and $g(\tilde{\nu} - \tilde{\upsilon}_{m(l)})$ are the amplitude of the mth normal mode of the lth species ($m(l)$) and corresponding band shape function (Gaussian, Lorentzian, Voight, etc.), and the summation is over all IR active normal modes for the lth species ($M(l)$). In the Fourier domain, the same expression can be re-written as $\int_{-\infty}^{\infty}\varepsilon_l(\tilde{\upsilon})e^{2\pi ik0} \sim d\tilde{\upsilon} = \sum_{m(l)}^{M(l)} A'm_{(l)}e^{2\pi ik\tilde{\upsilon}_{m(l)}}g_{m(l)}(k)$, where $A'_{m(l)}$ is the amplitude function in the phasor domain (proportional to $A_{m(l)}$) and $g_{m(l)}(k)$ is the line shape function (Gaussian, exponential, etc.). In summary, for any single chemical species, the entire IR spectra can be visualized in the phasor domain as a vector with a uniquely defined trajectory given by (a) relative intensities of the different vibrational modes, (b) their frequencies, and (c) their band shape functions. For any pixel belonging to a particular cell type or disease type in the IR data, the trajectory is ultimately governed by the concentration weighed summation of trajectories of the l species contributing to that pixel as given by eqs 8a and 8b:

$$u(k,x,y) = \sum_l c_l(x,y)L(x,y)\sum_{m(l)}^{M(l)} A_{m(l)} cos(2\pi k\tilde{\upsilon}_{m(l)})g_{m(l)}(k) \tag{8a}$$

$$v(k,x,y) = \sum_l c_l(x,y)L(x,y)\sum_{m(l)}^{M(l)} A_{m(l)}\sin(2\pi k\tilde{\upsilon}_{m(l)})g_{m(l)}(k) \tag{8b}$$

These equations collectively show that the phasor components are linearly proportional to the concentration of the lth chemical species, just like the absorbance spectra, with

coefficients that have oscillatory contributions. Thus, the phasor representation contains essentially the same information and linear dependence of absorption spectra; however, with its transformation properties, it makes the spectral domain significantly more sensitive to small spectral changes in absorption spectra. These properties make it especially attractive for IR analysis of biomedical samples where small differences typically characterize differences between cells or disease states. Compared to methods like second derivative analyses that also seek to highlight small differences between broadly similar IR spectra, the phasor representation does not degrade the signal-to-noise ratio (SNR).

Carcinomas are the most common type of human cancer, arising in epithelial cells and accounting for more than 80% of all cancer diagnoses. As a consequence, there is interest in understanding the role of epithelial cells and the surrounding tissue that is known collectively as the stroma. Many studies using IR imaging have focused on examining these two broad classes of components in tissue, and we consider their representative spectra first. Baseline-subtracted and normalized spectra from a benign prostate tissue sample are presented in Figure 2A. Sloping baselines in IR spectra arise from scattering effects, and we will subsequently discuss the implications of it for the phasor approach. The spectra are largely similar, with a common set of features since most biological materials are composed of the same elementary building blocks (i.e., nucleic acids, lipids, carbohydrates, and proteins). The corresponding transform domain data are presented in Figure 2B with the absolute value of the inverse Fourier transform, where a decaying beat pattern arising out of multiple IR bands can be observed, which is also apparent in the phasor trajectory (inset of Figure 2B). To differentiate between any two spectra, the angle between the two phasor vectors at different spatial frequencies can be used, which is defined as

$$\theta(k) = \cos^{-1}\left(\frac{(\overrightarrow{P_1}(k) \cdot \overrightarrow{P_2}(k))}{|\overrightarrow{P_1}(k)| \; |\overrightarrow{P_2}(k)|}\right) \tag{9}$$

which is presented in Figure 2C. From Figure 2C, a maximum separation between the epithelium and stroma is observed at $k = 0.01091$ with an angle of about 40 degrees between their phasor vectors. Figure 2D(i–iv) shows compass representations of the normalized phasor components for four different k values. Since the spectrum is a real function, at $k = 0$, v is identically zero for all spectra, and u is equal to the integrated intensity of the spectrum. Consequently, the normalized phasors align along the x axis at $k = 0$. They separate out at higher phasor frequencies, as seen in Figure 2D(ii–iv). These characteristics are the fundamental properties underlying the phasor approach to IR absorption spectra. Although the angle between the average epithelium and stromal phasors maximizes at $k = 0.01091$, the phasor values at higher k have lower values of SNR, which would not be obvious from the average spectra alone. Nonetheless, all the local maxima in the plot are good initial choices for the results demonstrated in the subsequent sections.

Although the application and interpretation seem relatively straightforward, there are additional complications in IR images from biomedical samples that arise due to the effects of mixed pixels,[24] intraclass biological heterogeneity,[25] scattering effects[26–29] and

experimental noise.[30–32] With these considerations, it is not immediately obvious whether the proposed approach can be useful for tissue segmentation. To evaluate its potential, we first consider the task of unsupervised classification that is common at the data exploratory and discovery stage of analyses. Briefly, in unsupervised methods, the goal is to segment data based on observed statistical patterns independent of any inputs from domain experts such as pathologists. Popular numerical methods include K-means,[33] hierarchical clustering,[34] or, frequently, manual thresholding on combinations of spectral indices. All these approaches are iterative and relatively slow for large biomedical datasets, presenting a data visualization challenge that is often required to examine the data for key features and outliers. The phasor technique, exploiting the speed of the FFT, can provide a fast alternative. The results of applying our approach are demonstrated in Figure 3 with a benign prostate tissue sample. Figure 3A shows the distribution of the absorption of the amide I band (1650 cm^{-1}), without baseline subtraction. Although it highlights the tissue, absorbance at a single frequency is typically not enough for delineating the contrast between cell types, such as glands and the adjoining stroma in epithelial cancers. Analogous to fluorescence-based phasor approaches, we generate contour plots of a 2D histogram of normalized u and v values (normalized to $u(k = 0)$), which are typically known as the "phasor plots" and are shown in Figure 3B. Briefly, we bin the $u(k)$ and $v(k)$ values for all the pixels in the IR data to generate a 2D histogram of every u and v pair in the image. These "phasor plots" can be interpreted both as an abundance within the tissue, wherein the density (phasor count) is a measure of the prevalence of pixels with the same characteristics, and the diversity in composition, wherein the separation between two phasor points is a measure of the difference in their spectra. A region can be selected in phasor plots such as shown by the bounded selections shown in Figure 3B. Mapping phasor values inside those bounds to the image reveals clusters, as shown in Figure 3C, which correspond to epithelial (green) and stroma (pink) as well as outlier pixels (red) and highly scattering pixels (like the ones at the edge of the glands, blue). It is also important to point out that this segmentation provides spectro-chemically distinguishable classes (as opposed to histologic classes commonly identified by morphology), which may or may not have physiologic relevance. Hence, we examine the average spectra that are derived from each cluster (Figure 3D). The spectra show differences in both the fine features associated with absorbance (which can arise from changes in concentration or path length) as well as broad, slowly varying variations (which arise from scattering).

To assess chemical changes, data preprocessing techniques are commonly applied to spectra, including those for denoising and baseline correction. A common method for biomedical analyses with IR spectra is to de-noise spectra based on the MNF transform.[18] The effect of MNF de-noising on the phasor-based classification method is presented in Figure SI12. As expected, it leads to lower classification noise due to decreased variances in the phasor space, which manifests as minor changes in the shape of the phasor distribution. In principle, Fourier de-noising methods, which can de-noise spectra by application of apodization functions in the k domain, can be adapted for our approach. Scattering also, most prominently, leads to a non-zero baseline and can also affect finer features of the spectra. Typically, pixels at the edges of the tissue have large scattering contributions since the typical thickness of histologic sections are comparable to IR wavelengths (3−10 μm),

and cellular features have the same dimensions.[35] Regardless of physical origin, scattering effects manifest as a broadband, slowly varying feature, whereas absorption modes result in relatively fine features corresponding to normal modes of chemical species. Consequently, it is expected that scattering effects will dominate the lower phasor frequencies, whereas the chemical contributions will dominate the higher phasor frequencies. This is demonstrated in Figure 4. While the effect of baseline subtraction (rubber-band baseline subtraction) is nominal in the higher phasor frequency ($k = 0.032$) (Figure 4A(i and ii)), the lower phasor frequency $\left(k = 7.94 \times 10^{-4}\right)$ is altered much more, and as can be seen in Figure 4B(iii and iv), previously unresolvable clusters can be resolved into two distinct “epithelial” and “stromal” clusters, as shown with the binary class maps in Figure 4C. An examination of the average normalized spectra from the above clusters reveals interesting spectral differences at 1740 and 1080 cm^{-1}, which correspond to ester carbonyl mode and phosphate vibrational modes, respectively. Collectively, Figure 4 demonstrates that with an appropriate choice of phasor frequency, it is possible to mitigate the effects of scattering in classification.

To demonstrate the generalizability and usefulness of the phasor approach, we apply it to a variety of samples and experimental conditions. First, we utilize measurements in both transmission and transflection modes.[36] On the sample preparation side, there are also two possible tissue processing metho—sFF and FFPE. Furthermore, tissue imaging has been widely reported for different spatial pixel sizes. A full discussion of these parameters is beyond the purview of this study; however, here, we examine the generalizability of our approach. Figure 5 shows two representative example—slarge surgical sections of FF prostate tissue that contain native distributions of cells, imaged at 5.5 μm pixel size in transflection mode, and a carefully curated TMA of FFPE breast tissue that represents different cell types in normal and diseased tissue, imaged at 1.1 μm pixel size in transmission mode. Figure 5A shows the H&E-stained section of tissue with prostate cancer (PCa) of two Gleason grades (GS),[37] GS = 3 (top) and GS = 5 (bottom), assessed by a board-certified pathologist. While the absorbance at the amide I mode (Figure 5B) does not display a significant contrast, the phasor distribution (Figure 5C, $k = 0.0032$) shows the presence of four clusters, whose projection back to the image allows an appreciation of the different domains in the sample (Figure 5D). Here, one cluster (labeled 3) corresponds largely to stroma and another (labeled 2) to epithelial cells that highlight benign and low-grade cancer glands (GS ≤ 3) (zoomed-in ROI Figure 5(i and ii)). Importantly, a different cluster (labeled 1) highlights the clinically important GS = 5 pattern. Finally, the cluster labeled 4 highlights texture within the stroma, which is not immediately obvious from the H&E-stained image. Thus, the phasor approach holds the potential to relate to known tissue components as well as can aid in discovery of novel components. It is interesting to examine the spectral features that distinguish the clusters. Figure 5I shows the average, baseline-corrected, and normalized spectra belonging to the pixels of each class. There is a difference in average spectra between cluster 1 and cluster 2 in the ester carbonyl peak and the phosphate vibrational modes, which are characteristic of lipids and the phosphodiester bonds in DNA/RNA. Application of the approach to breast tissue is illustrated by the example of four TMA cores, with two benign (top left and bottom right) and two cancerous cores (top right and bottom left) (Figure 5E). Again, the amide I absorbance image (Figure 5F) highlights some contrast between the morphological classes in the benign core but is not

very prominent in the others. The corresponding normalized phasor histogram is presented in Figure 5G for $k = 0.0032$. The shape of the phasor distribution and density are quite different from that of FF prostate, due both to the difference of tissue chemistry and the mode of imaging, but a clustering of phasor values can also be observed, revealing four clusters that largely correspond to benign and cancerous cells, stroma, and "other" classes of unknown origin, as shown in Figure 5H and zoomed-in figure (iii) and (iv).

Although Figure 5 is a simple means of visualizing and segmenting high-dimensional IR data, it is based only on the self-similarity of spectra, which might not always have histopathologic relevance. Furthermore, the choice of the phasor bounds can vary from user to user and may present difficulty in differentiating classes with very similar spectra. Hence, supervised analyses may be used on phasor data in a manner similar to that for absorption spectra. We trained a two-layer feed-forward artificial neural network with six histologic classes—alignant epithelium, benign epithelium, loose stroma, dense stroma, desmoplastic stroma, and others (necrosis and other entities). The class labels (~70,000) were assigned by consultation with expert pathologists and have been previously reported.[19] Analogous to the previously published work, MNF de-noising and rubber-band baseline subtraction were done on the data. The input to the network were the u and v phasor values at 12 different spatial frequencies (normalized to $k = 0$). The first layer consisted of 10 neurons with hyperbolic tan activation function, and the second layer had six neurons with softmax activation function. All the neurons in the network were fully connected, and training was achieved by optimizing the weights (W) and biases (b) of all the layers by minimizing the cross-entropy between the prediction and the target. Scaled conjugate backpropagation was used for minimizing the loss function and updating training variables. The total number of annotated pixels was randomly divided into a 70–30 ratio for training and validation, respectively. The chief consideration in this method is choosing the spatial frequencies for phasor values. We have adopted the following procedure for selection of phasor frequencies for the supervised classification results, as shown in Figure 6. First, we calculate the Fourier transform of the average spectra of annotated pixels of IR data for each class (1–6). These are subsequently used to calculate the angle between the following vectors: (1) average of all the classes (1–5) and others class (6); (2) epithelium (average of 1 and 2) and stroma (average of 3, 4, and 5); (3) benign (1) and malignant epithelium (2); (4) normal stroma (average of 3 and 4) and desmoplastic stroma (5); and (5) loose stroma (3) and dense stroma (4). The class labels are the same as that of the main text, i.e., 1 = benign epithelium, 2 = malignant epithelium, 3 = loose stroma, 4 = dense stroma, 5 = desmoplasia, and 6 = others. Figure SI3 shows the θ vs k plots for the above. Twelve frequencies were chosen as marked by the asterisks and are tabulated in SI Table 1, all of which correspond to local maxima. IR spectra of tissues are generally similar as the building blocks of natural biological materials are largely similar. Variations in their relative intensities and line shapes provide critical differences that allow typing and subtyping of classes of cells or diseases. Similarly, compositional differences between cell types and tissues of origin reside in small spectral variations. The exact k values used in this paper will not necessarily generalize to any classification task in any tissue given these differences; nevertheless, the strategy provided here and the features themselves can serve as good initial guesses for exploratory analyses. As expected, higher spatial frequencies are generally more informative

(resolving overlapping phasors) but noisy. Smaller spatial frequencies are dominated by intensity variations due to overall spectral shapes (once scattering is removed) and lacking in chemical contrast since most biomedical spectra are relatively similar. The results for supervised classification are demonstrated in Figure 6 for the breast cancer TMA. Figure 6A(i and ii), B(i and ii) shows the H&E-stained and classified images of a benign core that shows benign epithelial cells surrounded by loose stroma and intervening regions of dense stroma. Figure 6C(i and ii) shows the H&E and class images of malignant tumors with thin regions of intervening desmoplastic stroma, and Figure 6D(i and ii) shows the H&E and class images of thick regions of desmoplasia with localized cancer deposits from which the agreement between the H&E stains and IR classification can be visually appraised. The results are in good agreement with the previously published results, and we assessed its quantitative accuracy using receiver operator characteristic (ROC) curves for the six binary classifications (desired class vs all others) presented in Figure 6E (inset zoomed-in extreme left part). The accuracy of a classifier is quantified by the area under the curve (AUC), which is a measure of combined selectivity and specificity of a model (AUC = 1 is perfectly sensitive and specific, and AUC = 0.5 is a random predictor). The average AUC values for all the classes are equal to 0.9860, with the lowest value (0.9627) corresponding to desmoplastic stroma. The overall performance was also evaluated with a confusion matrix between the predicted class and the targeted class and is presented in Figure 6F. The accuracy can be evaluated with the values of off-diagonal elements, which in this case are low (highest confusion 1.1%). Comparing the results with figure 4 of ref 18 shows that the performance of our new algorithm is comparable to the results obtained with a random forest classifier trained with curated spectral metrics. A similar number of features (~25) were obtained in both these methods. This is not surprising since the information content of both these (quite different processing methods) is the same. We also caution that the accuracies reported here are not the accuracies for an IR imaging method applied to tissue but simply a test of our approach to understanding spectra against known values. A study that definitively provides diagnostic analyses would have to demonstrate the same on independent samples, samples that are of sufficient diversity[25] and more reflective of clinical practice.[38] Finally, other supervised classification methods like support vector machine or logistic regression can also be applied to phasor quantities.

The primary motivation for the current study was to achieve fast, automated dimensionality reduction of high-dimensional IR images. As shown, this can be useful for both unsupervised and supervised segmentation. The results presented in Figure 3 are similar in vein to the conventional phasor analysis of fluorescence lifetime data. However, unlike fluorescence lifetime data, IR spectral data are much richer in information and different in content. IR features arise from the frequencies, relative intensities, and band shapes of a large number of IR active modes together with the impacts of scattering. Therefore, it was not a priori obvious whether a phasor representation would be useful for IR data. In a typical workflow, a trained spectroscopist heuristically tries many combinations through an iterative, time-consuming process, which demands a lot of expertise and patience. Once the features have been identified, ML models can be trained, and the number and types of metrics can be fine-tuned. In this paper, we present a simpler, systematic procedure to achieve the same end goal. Unlike manual selection, PCA can also be employed for a

compact representation of the data. The phasor method can be advantageous over PCA. First, FFT algorithms are faster and scale favorably with large data sizes. Computations for PCA involve high-dimensional covariance calculations, for which the computational time can be very large for large datasets (TMAs). Second, phasor values can be independently calculated and combined because of the linearity of Fourier transforms. Third, principal components (PCs) may be dominated by scattering effects, which can be isolated into the low-frequency modes of the phasor representation. Unlike PCs, however, since the phasor components are oscillatory with complex contributions from the modes, it is not possible to identify what modes contribute the most to the separation in phasor space. Another aspect of both approaches is noise removal. Noise is distributed across the entire waveform. Therefore, selection of specific components (especially lower spatial frequency components) can lead directly to de-noising of data, which is similar to PCA-based noise rejection approaches and does not result in spatial compromises.[39] As discussed in the example application, this approach is likely to be useful for exploring complex classification problems where subtle changes in disparate modes are needed. For simple analyses, for example, which can be achieved using intensity ratios of a few modes, this approach is redundant and time-inefficient. Although the phasor approach is applicable to discrete frequency IR imaging data as well, its usefulness is questionable. This is because low-frequency resolution leads to a smaller phasor frequency range and thus poor resolution of features in the k domain (analogous to how higher retardance in FTIR is needed for higher resolution). The approach is similar in spirit to using a Gram–Schmidt approach for rapid change determination, as used for online FTIR spectroscopy and also proposed for imaging;[40] however, the Gram–Schmidt approach is more useful for assessing differences and does not have an explicit dependence of the absorbance in the transformed frequency domains.

CONCLUSIONS

Here, we present an easy and pictorial technique for dimensionality reduction that allows visualization and exploratory unsupervised analyses and can be used as inputs for a supervised ML model. A simple examination of phasor images leads to unsupervised segmentation, and using phasor values for supervised classification of IR imaging data shows good agreement with prior classification results. Although the premise of the phasor approach is known, its use for IR vibrational spectral analyses is shown to be an effective application type for biomedical data exploration, where small differences can dominate over large spectral regions. Since this is a data representation technique, it should be broadly applicable to other types of micro-spectroscopic datasets (spontaneous Raman, nano-IR, or photothermal IR).

Supplementary Material

Refer to Web version on PubMed Central for supplementary material.

ACKNOWLEDGMENTS

S.M. acknowledges the help provided by Prof. Shachi Mittal in using the tissue microarray data and Dr. Matthew Confer for discussions and reviewing the manuscript. We gratefully acknowledge the support from the National Institutes of Health via grants R01EB009745 and R01CA260830.

REFERENCES

(1). Baker MJ; Trevisan J; Bassan P; Bhargava R; Butler HJ; Dorling KM; Fielden PR; Fogarty SW; Fullwood NJ; Heys KA; Hughes C; Lasch P; Martin-Hirsch PL; Obinaju B; Sockalingum GD; Sulé-Suso J; Strong RJ; Walsh MJ; Wood BR; Gardner P; et al. Nat. Protoc. 2014, 9, 1771–1791. [PubMed: 24992094]

(2). Nasse MJ; Walsh MJ; Mattson EC; Reininger R; Kajdacsy-Balla A; Macias V; Bhargava R; Hirschmugl CJ Nat. Methods 2011, 8, 413–416. [PubMed: 21423192]

(3). Phal Y; Yeh K; Bhargava R Appl. Spectrosc. 2021, 75, 1067–1092. [PubMed: 33876990]

(4). Gerwert K; Schörner S; Großerueschkamp F; Kraeft AL; Schuhmacher D; Sternemann C; Feder IS; Wisser S; Lugnier C; Arnold D; Teschendorf C; Mueller L; Timmesfeld N; Mosig A; Reinacher-Schick A; Tannapfel A Eur. J. Cancer 2023, 182, 122–131. [PubMed: 36773401]

(5). Jonscher AK J. Phys. D: Appl. Phys. 1999, 32, R57.

(6). Redford GI; Clegg RM J. Fluoresc. 2005, 15, 805–815. [PubMed: 16341800]

(7). Digman MA; Caiolfa VR; Zamai M; Gratton E Biophys. J. 2008, 94, L14–L16. [PubMed: 17981902]

(8). Fereidouni F; Bader AN; Gerritsen HC Opt. Express 2012, 20, 12729–12741. [PubMed: 22714302]

(9). Cutrale F; Trivedi V; Trinh LA; Chiu CL; Choi JM; Artiga MS; Fraser SE Nat. Methods 2017, 14, 149–152. [PubMed: 28068315]

(10). Fu D; Xie XS Anal. Chem. 2014, 86, 4115–4119. [PubMed: 24684208]

(11). Robles FE; Wilson JW; Fischer MC; Warren WS Opt. Express 2012, 20, 17082–17092.

(12). Vergeldt FJ; Prusova A; Fereidouni F; Amerongen HV; Van As H; Scheenen TWJ; Bader AN Sci. Rep. 2017, 7, 861. [PubMed: 28408740]

(13). Stone HJ Opt. Soc. Am. 1962, 52, 998–1003.

(14). Kauppinen JK; Moffatt DJ; Cameron DG; Mantsch HH Appl. Opt. 1981, 20, 1866–1879. [PubMed: 20332848]

(15). Griffiths PR; De Haseth JA Fourier Transform Infrared Spectrometry; John Wiley & Sons, Inc.: Hoboken, NJ, 2007.

(16). Miljkovic M; Bird B; Diem M. Analyst 2012, 137, 3954–3964. [PubMed: 22811966]

(17). DeVetter BM; Kenkel S; Mittal S; Bhargava R; Wrobel TP Vib. Spectrosc. 2017, 91, 119–127.

(18). Reddy RK; Bhargava R Analyst 2010, 135, 2818–2825. [PubMed: 20830324]

(19). Mittal S; Wrobel TP; Walsh M; Kajdacsy-Balla A; Bhargava R Clin. Spectrosc. 2021, 3, 100006.

(20). Seshadri KS; Jones RN Spectrochim. Acta 1963, 19, 1013–1085.

(21). Stancik AL; Brauns EB Vib. Spectrosc. 2008, 47, 66–69.

(22). Davis BJ; Carney PS; Bhargava R Anal. Chem. 2010, 82, 3474–3486. [PubMed: 20392063]

(23). Davis BJ; Carney PS; Bhargava R Anal. Chem. 2010, 82, 3487–3499. [PubMed: 20392064]

(24). Bhargava R Anal. Bioanal. Chem. 2007, 389, 1155–1169. [PubMed: 17786414]

(25). Kwak JT; Reddy R; Sinha S; Bhargava R Anal. Chem. 2012, 84, 1063–1069. [PubMed: 22148458]

(26). Bhargava R; Wang S-Q; Koenig JL Appl. Spectrosc. 1998, 52, 323–328.

(27). Mohlenhoff B; Romeo M; Diem M; Wood BR Biophys. J. 2005, 88, 3635–3640. [PubMed: 15749767]

(28). Kohler A; Kirschner C; Oust A; Martens H Appl. Spectrosc. 2005, 59, 707–716. [PubMed: 16053536]

(29). Chan KLA; Kazarian SG Anal. Chem. 2013, 85, 1029–1036. [PubMed: 23244035]

(30). Bhargava R; Wang SQ; Koenig JL Appl. Spectrosc. 2000, 54, 486–495.
(31). Lasch P Chemom. Intell. Lab. Syst. 2012, 117, 100–114.
(32). Lux L; Phal Y; Hsieh PH; Bhargava R Appl. Spectrosc. 2022, 76, 105–117. [PubMed: 34643135]
(33). Lasch P; Haensch W; Naumann D; Diem M Biochim. Biophys. Acta, Mol. Basis Dis. 2004, 1688, 176–186.
(34). Hughes C; Iqbal-Wahid J; Brown M; Shanks JH; Eustace A; Denley H; Hoskin PJ; West C; Clarke NW; Gardner PJ Biophotonics 2013, 6, 73–87. [PubMed: 23125109]
(35). Davis BJ; Scott Carney P; Bhargava R Anal. Chem. 2011, 83, 525–532. [PubMed: 21158469]
(36). Perez-Guaita D; Heraud P; Marzec KM; de la Guardia M; Kiupel M; Wood BR Analyst 2015, 140, 2376–2382. [PubMed: 25695358]
(37). van Leenders G; van der Kwast TH; Grignon DJ; Evans AJ; Kristiansen G; Kweldam CF; Litjens G; McKenney JK; Melamed J; Mottet N; Paner GP; Samaratunga H; Schoots IG; Simko JP; Tsuzuki T; Varma M; Warren AY; Wheeler TM; Williamson SR; Iczkowski KA Am. J. Surg. Pathol. 2020, 44, e87–e99. [PubMed: 32459716]
(38). Bhargava R Annu. Rev. Anal. Chem. 2023, 16, 205–230.
(39). Bhargava R; Ribar T; Koenig JL Appl. Spectrosc. 1999, 53, 1313–1322.
(40). Bhargava R; Levin IW Appl. Spectrosc. 2004, 58, 995–1000. [PubMed: 15324507]

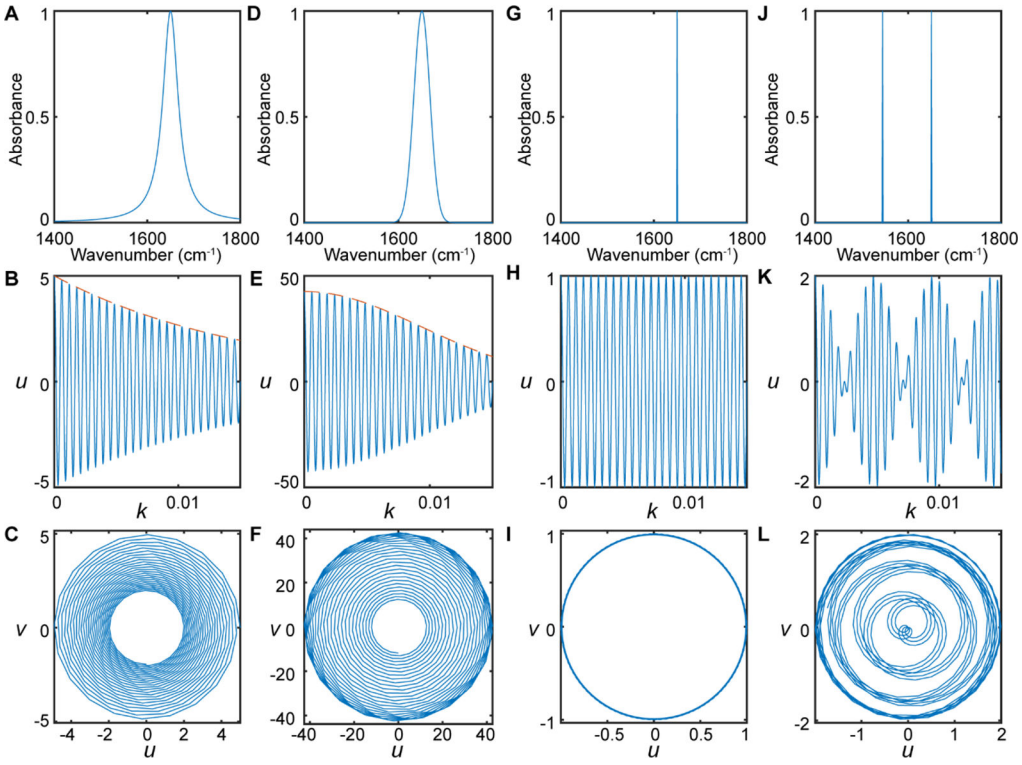

Figure 1.

Mathematical formalism of the phasor approach with representative simulated IR spectra. (A–C) Lorentzian spectrum; (A) spectrum, (B) u, and (C) trajectory of the phasor in k space. (D–F) Gaussian spectrum; (D) spectrum, ϵ u, and (F) trajectory of the phasor in k space. (G–I) Dirac delta spectrum; (G) spectrum, (H) u, and (I) trajectory of the phasor in k space. (J–L) Dirac delta pair; (J) spectrum, (K) u, and (L) trajectory of the phasor in k space.

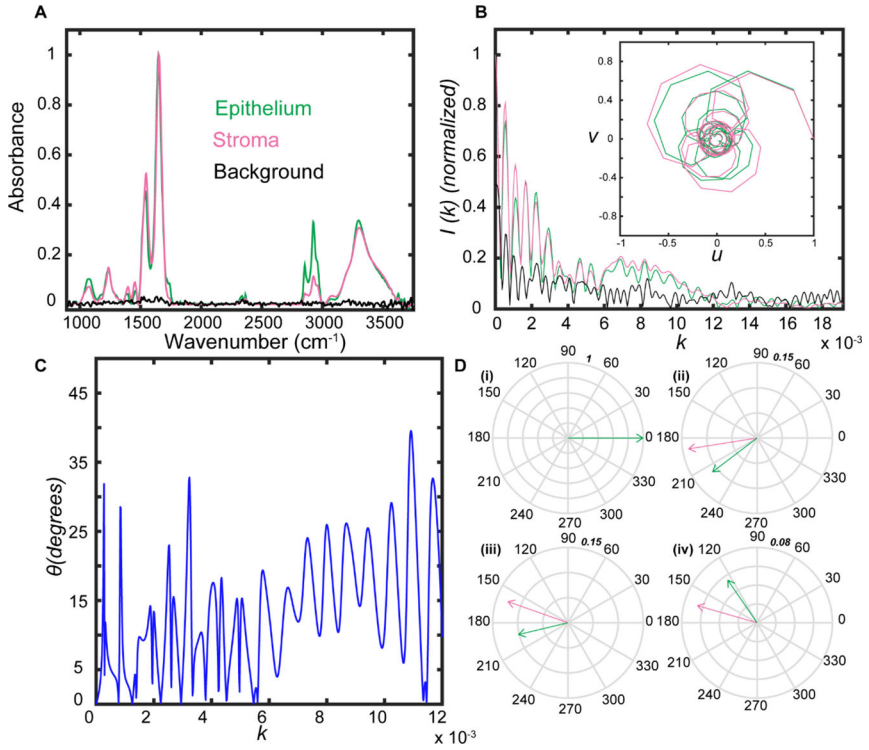

Figure 2.

Key characteristics of phasor-based analyses and segmentation. (A) Average baseline-subtracted spectra of two different histologic classes in prostate tissue-epithelial cells (green) and stroma (pink) normalized to amide I (1650 cm^{-1}) and unnormalized background (black). (B) Absolute value of the inverse Fourier transform of the three spectra presented in (A). The epithelial and stromal data have been normalized to the $k = 0$ value. The background has been scaled 500 times for visual appraisal. Inset B shows the phasor trajectory. (C) θ as defined in the main text. (D) Compass plots of the vectorial representation: (i) $k = 0$, (ii) $k = 0.0002747$, (iii) $k = 0.003235$, and (iv) $k = 0.01091$. All the vectors are normalized to u ($k = 0$).

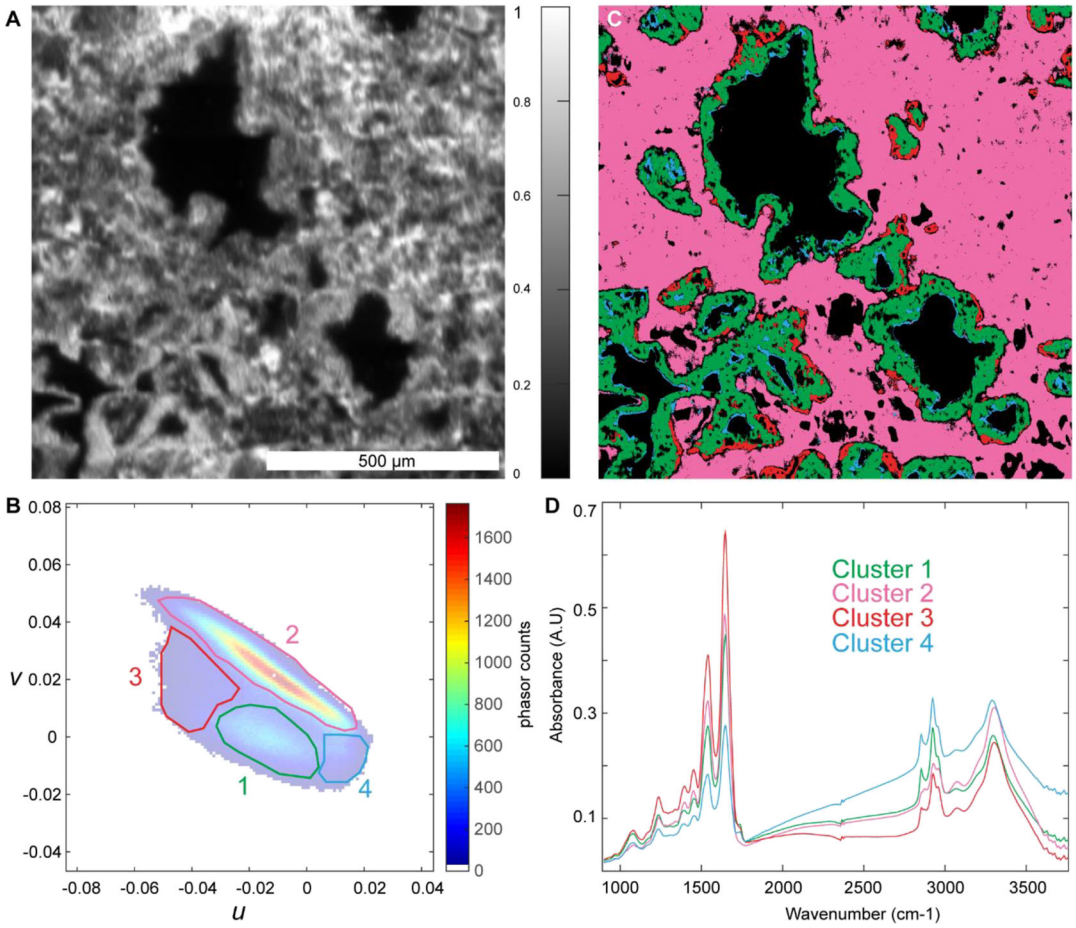

Figure 3.

Unsupervised classification of IR hyperspectral images using the phasor representation. (A) Single band IR image (1650 cm^{-1}). (B) Phasor histogram plots with freeform selection areas ($k = 0.0032$). (C) Classified image obtained from each of the clusters (color coded). (D) Average spectra of each of the clusters.

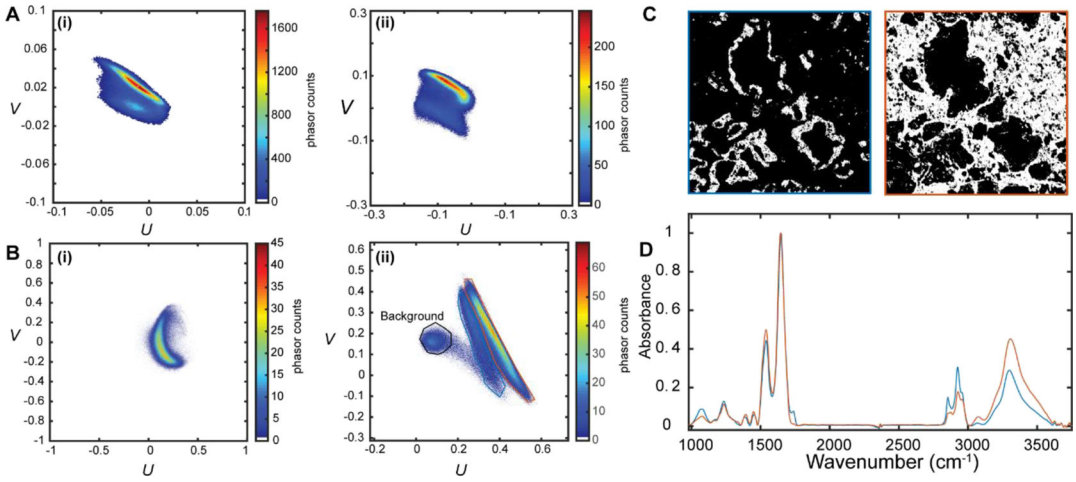

Figure 4.

Effect of baseline removal using phasor processing. (A) (i) Phasor representation of $k = 0.0032$ without baseline subtraction and (ii) phasor representation of $k = 0.0032$ with baseline subtraction. (B) (i) Phasor representation of $k = 0.0002747$ without baseline subtraction and (ii) phasor representation of $k = 0.0002747$ with baseline subtraction. (C) Classified area from freeform selection of B (ii). (D) Average spectra of the selected clusters normalized to amide I intensity.

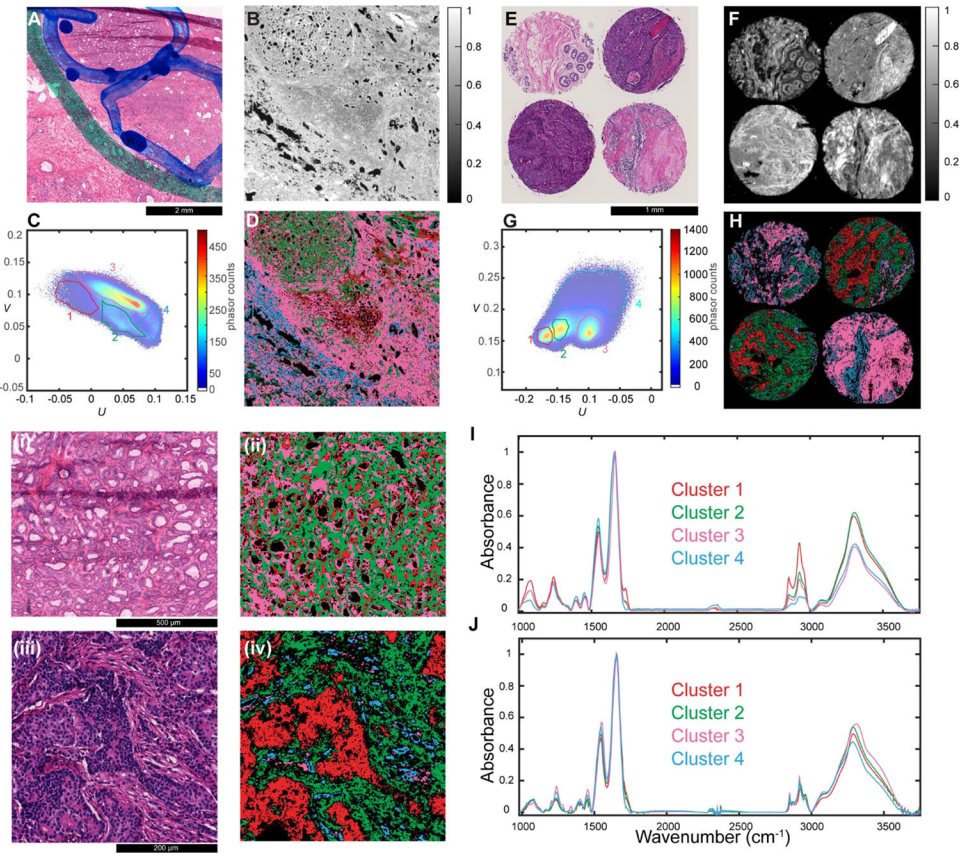

Figure 5.

Unsupervised classification results. (A–D) (i and ii), (I) Results for fresh frozen prostate tissue. (A) Adjacent H&E-stained section, (B) amide I (1650 cm^{-1}) image, (C) phasor plot with the location of the clusters (color coded) highlighted, (D) classified image, (i) H&E image of ROI and (ii) classified image of ROI, and (I) average spectra of the different classes. (E–H) (iii and iv), (J) Results for FFPE breast cancer TMA cores. (E) Adjacent H&E-stained section, (F) amide I (1650 cm^{-1}) image, (G) phasor plot with the location of the clusters (color coded) highlighted, (H) classified image, (iii) H&E image of ROI and (iv) classified image of ROI, and (J) average spectra of the different classes.

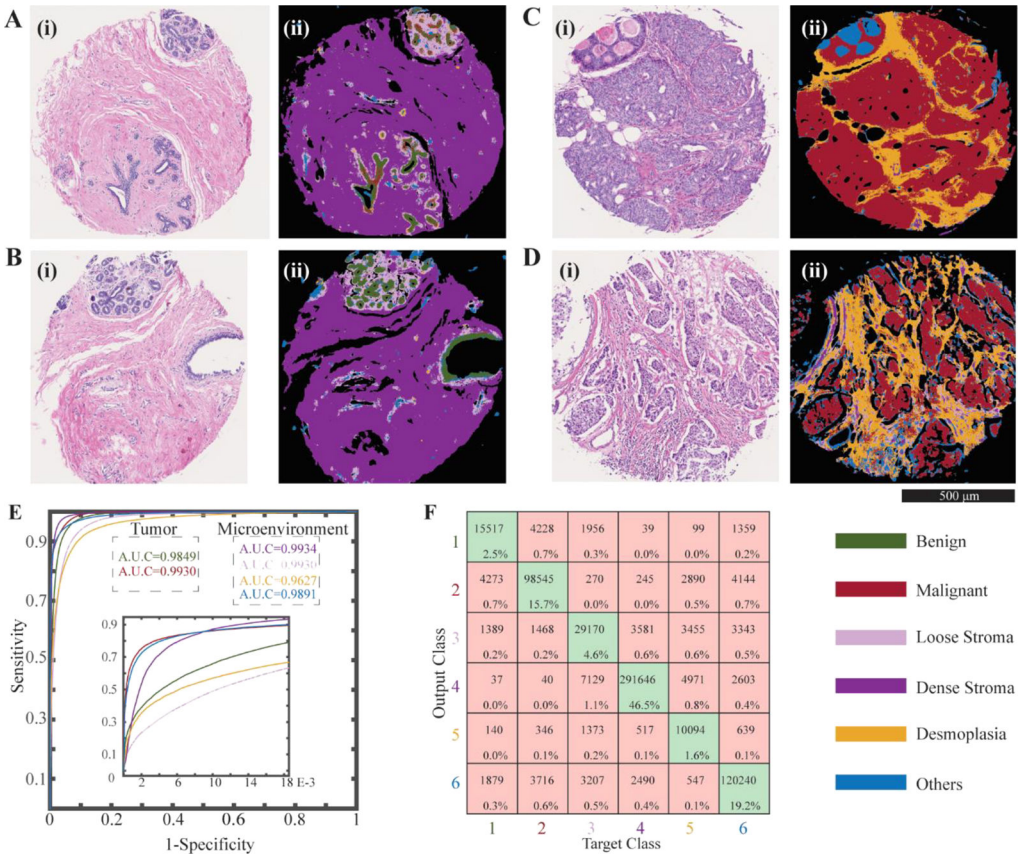

Figure 6.

Supervised classification of IR hyperspectral images using phasor representation. (A) (i) H&E and (ii) class image of benign. (B) (i) H&E and (ii) class image of benign, (C) (i) H&E and (ii) class image of cancer, (D) (i) H&E and (ii) class image of cancer with desmoplasia. (E) ROC curves of classification (AUC = area under the curve) with the inset showing the extreme left end of ROC. (F) Confusion matrix.